

NON-INTRUSIVE PODI-ROM FOR PATIENT-SPECIFIC AORTIC BLOOD FLOW IN PRESENCE OF A LVAD DEVICE

M. GIRFOGLIO^{1,*}, F. BALLARIN¹, G. INFANTINO², F. NICOL³, A. MONTALTO³, G. ROZZA¹, R. SCROFANI⁴,
M. COMISSO³, AND F. MUSUMECI³

ABSTRACT. Left ventricular assist devices (LVADs) are used to provide haemodynamic support to patients with critical cardiac failure. Severe complications can occur because of the modifications of the blood flow in the aortic region. In this work, the effect of a continuous flow LVAD device on the aortic flow is investigated by means of a non-intrusive reduced order model (ROM) built using the proper orthogonal decomposition with interpolation (PODI) method. The full order model (FOM) is represented by the incompressible Navier-Stokes equations discretized by using a Finite Volume (FV) technique, coupled with three-element Windkessel models to enforce outlet boundary conditions in a multi-scale approach. A patient-specific framework is proposed: a personalized geometry reconstructed from Computed Tomography (CT) images is used and the individualization of the coefficients of the three-element Windkessel models is based on experimental data provided by the Right Heart Catheterization (RCH) and Echocardiography (ECHO) tests. Pre-surgery configuration is also considered at FOM level in order to further validate the model. A parametric study with respect to the LVAD flow rate is considered. The accuracy of the reduced order model is assessed against results obtained with the full order model.

1. INTRODUCTION

Left ventricular assist devices (LVADs) provide full or partial mechanical circulatory support to the left ventricle of the heart. LVADs are increasingly used as both bridge to transplantation (BTT) and destination therapy (DT), for the treatment of patients with advanced heart failure (HF) refractory to maximal medical therapy [1, 51, 33]. The use of LVADs has been associated with an increased risk of thrombus formation in the aortic region because of the formation of stagnation points and recirculation zones; indeed, while first generation devices provided pulsatile flows, current LVADs produce continuous flow (cf-LVADs). This constant flow to the aortic root may lead to decreased excursion or even complete closure of the aortic valve (AV), particularly at high pump speeds. The resultant stasis in the aortic root forms a nidus for clot formation. Aortic root thrombosis has been recognized as a major complication of cf-LVAD therapy which frequently necessitates device exchange in eligible patients to restore forward flow and prevent embolic stroke [15, 14, 25, 4].

Several works deal with the computational investigation of the hemodynamics in the aortic region in the presence of a LVAD device, both in a single configuration [8] and varying of physical (LVAD flow rate [5, 40]) and geometrical (cannula angle [27, 45, 30, 31, 43] and anastomosis position [39, 38, 32, 13, 45, 30, 40, 10, 2, 9, 5, 10, 56]) parameters. In all these works, high fidelity full order models (FOMs) are used, based on either finite element and finite volume simulations.

Reduced order models (ROMs) (see, e.g., [46, 26, 6, 7]) have been proposed as an efficient tool to approximate full order systems by significantly reducing the computational cost required to obtain numerical solutions in a parametric setting. The basic idea on which ROM is based is that often the parametric dependence of the problem at hand has an intrinsic dimension much lower than the number of degrees of freedom of the discretized system. In order to reach this dimensionality reduction, a database of several solutions is first collected by solving the original high fidelity model for different physical and/or geometrical parameters (*offline phase*).

¹SISSA, SCUOLA INTERNAZIONALE SUPERIORE DI STUDI AVANZATI, AREA DI MATEMATICA, MATHLAB TRIESTE, ITALY.

²POLITECNICO DI TORINO, COLLEGIO DI INGEGNERIA MATEMATICA, MODELLI MATEMATICI E SIMULAZIONI NUMERICHE, TORINO, ITALY

³AZIENDA OSPEDALIERA SAN CAMILLO, UNIT OPERATIVA COMPLESSA DI CARDIOCHIRURGIA E CHIRURGIA DEI TRAPIANTI, ROMA, ITALY

⁴AZIENDA OSPEDALIERA FBF LUIGI SACCO, DIPARTIMENTO DI CARDIOCHIRURGIA, MILANO, ITALY

E-mail addresses: mgirfogl@sissa.it, fballarin@sissa.it, giuseppe.infantino@studenti.polito.it, nicolo.francy84@hotmail.it, andrea.montalto@libero.it, grozza@sissa.it, roberto.scrofani@asst-fbf-sacco.it, marina.comisso@gmail.com, fr.musumeci@gmail.com.

2010 *Mathematics Subject Classification.* 78M34, 97N40, 35Q35.

Key words and phrases. LVAD, aortic hemodynamics, non intrusive model reduction, data-driven techniques.

*Corresponding Author.

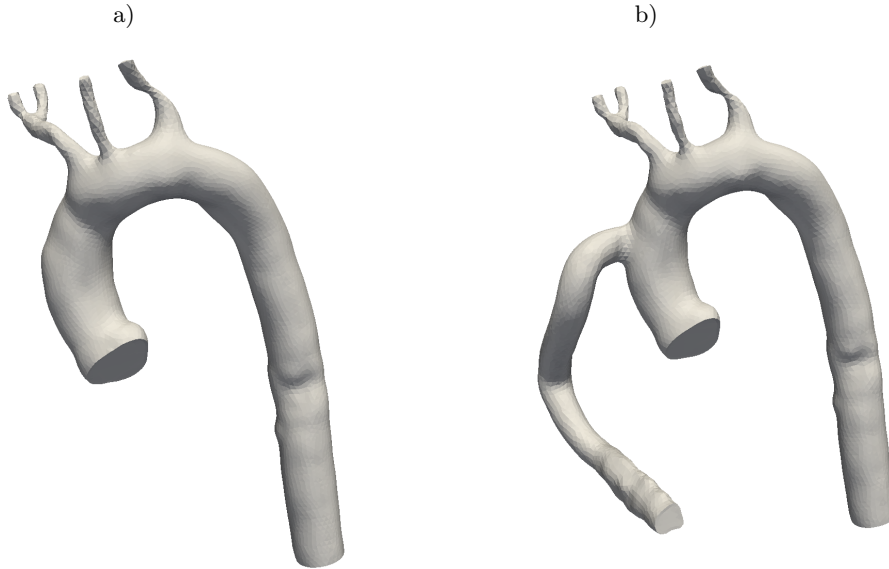


FIGURE 1. Patient specific aorta models obtained from CT images: a) Pre-surgery configuration, b) Post-surgery configuration.

Then, all the solutions are combined and compressed in order to build the space onto which we can project the solution manifold and efficiently compute the solutions for the new parameters (*online phase*).

In this work, a data-driven reduced order model based on the proper orthogonal decomposition with interpolation (PODI) method [11] is used for the investigation of the modifications to aortic blood flow patterns induced by the presence of the outflow cannula of a LVAD device. PODI is an equation-free method based on proper orthogonal decomposition capable to build a reduced order model without any knowledge about the equations of the original problem. Therefore, this method does not require information about the full order formulation and not even modifications to the numerical solver. Data-driven non-intrusive ROMs have been widely used within industrial applications framework (see, e.g. [52]). In our application, the parametrization is applied with respect to the flow rate provided by the LVAD device. The open-source finite volume solver OpenFOAM [54] is used to generate the FOM solutions which are then used as a training set for the ROM. In order to obtain a model able to reproduce clinical configurations, geometry is reconstructed from patient-specific Computed Tomography (CT) images. Moreover, a multi-scale approach was adopted by coupling three-element Windkessel models [55], used as boundary conditions for the aorta model, and which coefficients are estimated by using experimental data provided by Right Heart Catheterization (RHC) and Echocardiography (ECHO) tests. Pre-surgery configuration is also considered in order to further validate the FOM and the estimation procedure. Therefore, a complete patient-specific framework is proposed. To the best of our knowledge, parametric ROM for modeling realistic aortic flow in presence of LVAD devices is introduced in this paper for the first time.

The work is organized as follows. In Sec. 2 materials and methods are presented and in Sec. 3 the achieved results are introduced and discussed. Finally, in Sec. 4 conclusions and perspectives are provided.

2. CLINICAL DATA AND DISCRETIZATION BY FULL ORDER AND REDUCED ORDER MODELS

2.1. Clinical data. In this work a patient, a 66 years old man, is considered. CT, RHC and ECHO tests have been carried out both in pre-surgery and post-surgery (i.e., after receiving the LVAD device) configuration. The LVAD implanted is the Heartmate 3TM Left Ventricular Assist System [53].

2.2. Geometrical model. Real patient-specific aorta models were reconstructed from CT images by using the open source medical image analysis software 3D Slicer[®] (<http://www.slicer.org>). The models include the ascending aorta, brachiocephalic artery, right subclavian artery, right common carotid artery, left common carotid artery, left subclavian artery and descending aorta, and, in the post-surgery configuration, the outflow cannula of the LVAD device as well, as shown in Fig. 1.

PAS [mmHg]	PAD [mmHg]	PAM [mmHg]	CO [l/min]	SV [ml]
108	66	78	5.63	55

TABLE 1. Pre-surgery configuration: experimental data obtained by the RHC and ECHO tests. PAS = systolic arterial pressure, PAD = diastolic arterial pressure, PAM = average arterial pressure, CO = average cardiac flow rate, SV = stroke volume.

2.3. The full order model (FOM). In this Section we briefly introduce the mathematical model, i.e. the incompressible Navier-Stokes equations, with proper boundary conditions as well as the space and time discretization adopted.

2.3.1. The mathematical problem: Navier-Stokes equations. We consider the motion of the blood in a time-independent domain Ω over a time interval of interest $(t_0, t^*]$. The flow is described by the incompressible Navier-Stokes equations

$$(1) \quad \rho \partial_t \mathbf{u} + \rho \nabla \cdot (\mathbf{u} \otimes \mathbf{u}) - \nabla \cdot \boldsymbol{\sigma} = 0 \quad \text{in } \Omega \times (t_0, t^*],$$

$$(2) \quad \nabla \cdot \mathbf{u} = 0 \quad \text{in } \Omega \times (t_0, t^*],$$

endowed with proper boundary conditions. $\rho = 1060 \text{ Kg/m}^3$ is the blood density, \mathbf{u} is the blood velocity, ∂_t denotes the time derivative, $\boldsymbol{\sigma}$ is the Cauchy stress tensor. Equation (1) represents the conservation of the linear momentum, while eq. (2) represents the conservation of the mass. In this work, the blood is considered as a Newtonian fluid and $\boldsymbol{\sigma}$ can be written as

$$(3) \quad \boldsymbol{\sigma}(\mathbf{u}, p) = -p\mathbf{I} + \mu(\nabla \mathbf{u} + \nabla \mathbf{u}^T),$$

where p is the pressure and $\mu = 0.004 \text{ Pa} \cdot \text{s}$ is the blood *dynamic* viscosity. For the sake of convenience, we also define the viscous stress tensor $\boldsymbol{\tau}$ as follows

$$(4) \quad \boldsymbol{\tau}(\mathbf{u}) = \mu(\nabla \mathbf{u} + \nabla \mathbf{u}^T).$$

Notice that by plugging (3) into eq. (1), eq. (1) can be rewritten as

$$(5) \quad \rho \partial_t \mathbf{u} + \rho \nabla \cdot (\mathbf{u} \otimes \mathbf{u}) + \nabla p - \mu \Delta \mathbf{u} = \mathbf{f} \quad \text{in } \Omega \times (t_0, t^*].$$

In order to investigate the blood flow patterns, we introduce the Wall Shear Stress (WSS) defined in the following way

$$(6) \quad WSS = \boldsymbol{\tau}_w \cdot \mathbf{n},$$

where \mathbf{n} is the unit normal vector and $\boldsymbol{\tau}_w$ is the tangential component of the wall viscous stress tensor. When the flow is pulsatile, it is useful to make reference to the Time Averaged WSS (TAWSS),

$$(7) \quad TAWSS = \frac{1}{T} \int_0^T WSS \, dt.$$

Finally, in order to characterize the flow regime under consideration, we define the Reynolds number as

$$(8) \quad Re = \frac{UL}{\nu},$$

where $\nu = \mu/\rho$ is the *kinematic* viscosity of the blood, and U and L are characteristic macroscopic velocity and length, respectively. For a blood flow in a cylindrical vessel, U is the mean sectional velocity and L is the diameter.

2.3.2. Boundary conditions. Experimental measurements obtained by the RHC and ECHO tests are reported in Tables 1 and 2 for pre-surgery and post-surgery configuration respectively. They are used in order to enforce realistic boundary conditions. For clinical reasons, four different tests are available for the post-surgery configurations whilst only one for the pre-surgery configuration. Note that RHC and ECHO tests provided measurements related to the pulmonary circulation as well. However, these data are not reported because they do not affect the model used in this work, that deals with the systemic compartment only. In Table 3 we report the values of boundaries cross-sectional areas.

	PF [l/min]	ω [rpm]	PAM [mmHg]
Test 1	4.1	5400	78
Test 2	4.2	5600	90
Test 3	4.5	6000	100
Test 4	5	5600	83

TABLE 2. Post-surgery configuration: experimental data obtained by the RHC and ECHO tests. PF = LVAD flow rate, ω = pump speed, PAM = average arterial pressure.

	A [cm ²]
Outflow cannula	1.3
Ascending aorta	6.42
Right subclavian artery	0.156
Right common carotid artery	0.246
Left common carotid artery	0.168
Left subclavian artery	0.446
Descending aorta	3.68

TABLE 3. Values of boundaries cross-sectional areas.

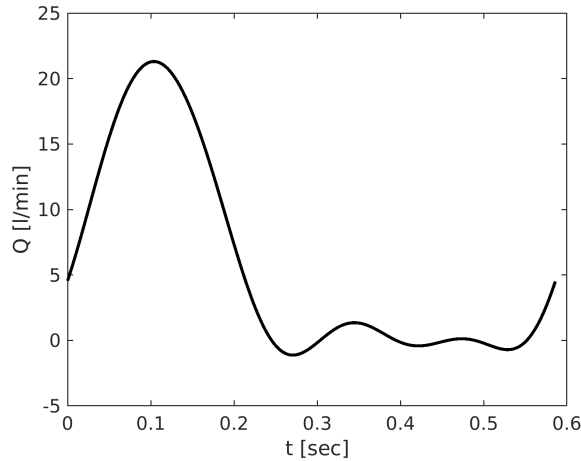


FIGURE 2. Aortic inflow waveform enforced in the pre-surgery case.

In the pre-surgery configuration, a realistic flow rate Q waveform was enforced on the ascending aorta section (Figure 2). The amplitude of the flow waveform has been set according to the average flow rate over the cardiac cycle, CO ,

$$(9) \quad CO = \frac{1}{T} \int_0^T Q dt,$$

measured by the RHC test. The value of a period of the cardiac cycle, T , is obtained as

$$(10) \quad T = \frac{SV}{CO},$$

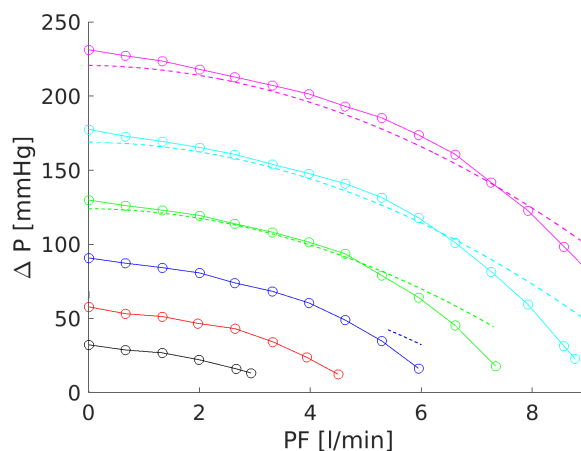
where SV is the stroke volume measured by the ECHO test.

On the other hand, in the post-surgery configuration, the LVAD flow rate, PF , has been used as inlet boundary condition applied to the outflow cannula section. Note that the aortic valve is closed during all the cardiac cycle, i.e. the cardiac flow rate is supplied by the LVAD device only and the ascending aorta section is treated as a wall. In Figure 3, the pressure head (ΔP) - volume flow rate (PF) curves for the Heartmate 3TM Left Ventricular Assist System [53] at several pump speed values ω are shown. The basic pump dynamics can,

K_A [mmHg/rpm ²]	K_B [mmHg · l/min/rpm]	K_C [mmHg · l ² /rpm ²]
3.45e-6	-5.9e-5	-1.45

TABLE 4. Parameter settings for the pump dynamics (eq. 11).

	ΔP [mmHg]
Test 1	75
Test 2	81.3
Test 3	93.3
Test 4	70.4

TABLE 5. ΔP values based on eq. 11 for all the tests under consideration.FIGURE 3. Pressure head (ΔP) - volume flow rate (PF) curves (continuous line with circles) and analytical fitting (dashed line) based on eq. 11 for Heartmate 3TM [53] pump at several pump speed values: $\omega = 3000$ rpm (black), $\omega = 4000$ rpm (red), $\omega = 5000$ rpm (blue), $\omega = 6000$ rpm (green), $\omega = 7000$ rpm (cyan), and $\omega = 8000$ rpm (magenta).

in principle, be described in the following way [50]

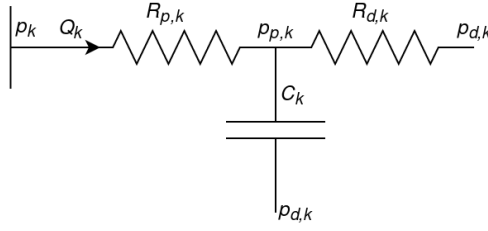
$$(11) \quad \Delta P = K_A \omega^2 + K_B \omega \cdot PF + K_C PF^2,$$

where K_A , K_B and K_C are constants which depend on pump design. After some numerical experiments, we found that the coefficients given in Table 4 provide an acceptable fit as showed in Figure 3. We note that a better agreement could be obtained by considering more complex equations in order to take into account nonlinear effects [50]. Based on the analytical fitting 11, we can compute the values of ΔP for the all the tests under consideration (see Table 5). The analytical fitting 11 will be also used in Sec. 3.2 in order to compute ω at given PF and ΔP .

Outflow boundary conditions were applied at each outlet of the model, right subclavian artery, right common carotid artery, left common carotid artery, left subclavian artery and descending aorta, by using a three-element Windkessel RCR model [55]. The Windkessel model consists of a proximal resistance $R_{p,k}$, a compliance C_k , and a distal resistance $R_{d,k}$, for each outlet k (Figure 4). The downstream pressure, p_k , is expressed through the following DAE system:

$$(12) \quad \begin{cases} C_k \frac{dp_{p,k}}{dt} + \frac{p_{p,k} - p_{d,k}}{R_{d,k}} = Q_k, \\ p_k - p_{p,k} = R_{p,k} Q_k, \end{cases}$$

where Q_k is the flow rate, and $p_{p,k}$ and $p_{d,k}$ are the proximal and the distal pressure, respectively. The total

FIGURE 4. Three-element Windkessel model for the generic outlet k

T [s]	RVS [dyne · s/cm ⁵]	C [cm ⁵ /dyne]
0.586	1105	9.85e-4

TABLE 6. Pre-surgery configuration: quantities computed by the experimental data reported in Tab. 1. T = period of the cardiac cycle (eq. 10), RVS = system vascular resistance (eq. 14), C = aortic compliance (eq. 16).

resistance, $R_k = R_{p,k} + R_{d,k}$, was evaluated according to the rules for a parallel circuit

$$(13) \quad R_k = RVS \frac{\sum_k A_k}{A_k},$$

where A_k is the cross-sectional area (see Table 3) and RVS is the systemic vascular resistance estimated as follows

$$(14) \quad RVS = \begin{cases} \frac{PAM}{CO}, & \text{in the pre-surgery case} \\ \frac{PAM}{PF}, & \text{in the post-surgery case} \end{cases}$$

where PAM is the average arterial pressure measured by the RHC test (see Tables 1 and 2). For each outlet k , we assumed [34]

$$(15) \quad \frac{R_{p,k}}{R_k} = 0.056.$$

On the other hand, the aortic compliance, C , can be estimated as follows [12]:

$$(16) \quad C = \frac{PAS - PAD}{SV}$$

where PAS and PAD are the systolic and the diastolic pressure measured by the RCH test in the pre-surgery configuration, respectively (see Table 1). It should be noted that such value is also used in the post-surgery configuration. Finally, the compliance C_k related to the outlet k was evaluated according to the rules for a parallel circuit

$$(17) \quad C_k = C \frac{A_k}{\sum_k A_k}.$$

Table 6 shows the values of T , RVS and C computed by using eqs. (10), (14), and (16), respectively, for the pre-surgery configuration. Table 7 shows the values of RVS computed by using eq. (14) for the post-surgery configuration. Finally, tables 8 and 9 report the values of Windkessel coefficients for the pre-surgery and post-surgery configurations, respectively.

2.3.3. Space and temporal discretization. For the space discretization of problems (2)-(5), we adopt the Finite Volume (FV) approximation that is derived directly from the integral form of the governing equations. We have used the finite volume C++ library OpenFOAM[®] [54]. We partition the computational domain Ω (i.e., the patient-specific geometrical models in Figure 1) into cells or control volumes Ω_i , with $i = 1, \dots, N_c$, where N_c is the total number of cells in the mesh. Let \mathbf{A}_j be the surface vector of each face of the control volume.

The integral form of eq. (5) for each volume Ω_i is given by:

	RVS [dyne · s/cm ⁵]
Test 1	1522
Test 2	1714
Test 3	1778
Test 4	1328

TABLE 7. Post-surgery configuration: system vascular resistance (eq. 14) computed by the experimental data reported in Tab. 2.

k	$R_{p,k}$ [dyne · s/cm ⁵]	$R_{d,k}$ [dyne · s/cm ⁵]	C_k [cm ⁵ /dyne]
Right subclavian artery	1.84e3	3.11e4	3.26e-5
Right common carotid artery	1.23e3	2.07e4	5.16e-5
Left common carotid artery	1.78e3	3.01e4	3.52e-5
Left subclavian artery	7.09e2	1.19e4	9.35e-5
Descending aorta	7.8e1	1.31e3	7.72e-4

TABLE 8. Pre-surgery configuration Windkessel coefficients: proximal resistance $R_{p,k}$, distal resistance $R_{d,k}$ and compliance C_k , for each outlet k .

	k	$R_{p,k}$ [dyne · s/cm ⁵]	$R_{d,k}$ [dyne · s/cm ⁵]
Test 1	Right subclavian artery	2.56e3	4.32e4
	Right common carotid artery	1.63e3	2.74e4
	Left common carotid artery	2.38e3	4e4
	Left subclavian artery	8.96e2	1.51e4
	Descending aorta	1.08e2	1.83e3
Test 2	Right subclavian artery	2.88e3	4.86e4
	Right common carotid artery	1.83e3	3.08e4
	Left common carotid artery	2.68e3	4.51e4
	Left subclavian artery	1.01e3	1.7e4
	Descending aorta	1.22e2	2.06e3
Test 3	Right subclavian artery	2.99e3	5.05e4
	Right common carotid artery	1.9e3	3.2e4
	Left common carotid artery	2.78e3	4.68e4
	Left subclavian artery	1.04e3	1.76e4
	Descending aorta	1.27e2	2.14e3
Test 4	Right subclavian artery	2.19e3	3.68e4
	Right common carotid artery	1.39e3	2.33e4
	Left common carotid artery	2.03e3	3.42e4
	Left subclavian artery	7.64e2	1.29e4
	Descending aorta	9.25e1	1.56e3

TABLE 9. Post-surgery configuration Windkessel coefficients: proximal resistance $R_{p,k}$ and distal resistance $R_{d,k}$, for each outlet k .

$$(18) \quad \rho \int_{\Omega_i} \frac{\partial \mathbf{u}}{\partial t} d\Omega + \rho \int_{\Omega_i} \nabla \cdot (\mathbf{u} \otimes \mathbf{u}) d\Omega - \mu \int_{\Omega_i} \Delta \mathbf{u} d\Omega + \int_{\Omega_i} \nabla p d\Omega = 0.$$

By applying the Gauss-divergence theorem, eq. (18) becomes:

$$(19) \quad \rho \int_{\Omega_i} \frac{\partial \mathbf{u}}{\partial t} d\Omega + \rho \int_{\partial\Omega_i} (\mathbf{u} \otimes \mathbf{u}) \cdot d\mathbf{A} - \mu \int_{\partial\Omega_i} \nabla \mathbf{u} \cdot d\mathbf{A} + \int_{\partial\Omega_i} p d\mathbf{A} = 0.$$

Each term in eq. (19) is approximated as follows:

- *Gradient term:*

$$(20) \quad \int_{\partial\Omega_i} p d\mathbf{A} \approx \sum_j p_j \mathbf{A}_j,$$

where p_j is the value of the pressure relative to centroid of the j^{th} face. The face center pressure values p_j are obtained from the cell center values by means of a linear interpolation scheme.

- *Convective term:*

$$(21) \quad \int_{\partial\Omega_i} (\mathbf{u} \otimes \mathbf{u}) \cdot d\mathbf{A} \approx \sum_j (\mathbf{u}_j \otimes \mathbf{u}_j) \cdot \mathbf{A}_j = \sum_j \varphi_j \mathbf{u}_j, \quad \varphi_j = \mathbf{u}_j \cdot \mathbf{A}_j,$$

where \mathbf{u}_j is the fluid velocity relative to the centroid of each control volume face. In (21), φ_j is the convective flux associated to \mathbf{u} through face j of the control volume. The convective flux at the cell faces is obtained by a linear interpolation of the values from the adjacent cells. Also \mathbf{u} needs to be approximated at cell face j in order to get the face value \mathbf{u}_j . Different interpolation methods can be applied: central, upwind, second order upwind and blended differencing schemes [29]. In this work, we make use of a second order upwind scheme.

- *Diffusion term:*

$$\int_{\partial\Omega_i} \nabla \mathbf{u} \cdot d\mathbf{A} \approx \sum_j (\nabla \mathbf{u})_j \cdot \mathbf{A}_j,$$

where $(\nabla \mathbf{u})_j$ is the gradient of \mathbf{u} at face j . We are going to briefly explain how $(\nabla \mathbf{u})_j$ is approximated with second order accuracy on structured, orthogonal meshes. Let P and Q be two neighboring control volumes. The term $(\nabla \mathbf{u})_j$ is evaluated by subtracting the value of velocity at the cell centroid on the P -side of the face, denoted with \mathbf{u}_P , from the value of velocity at the centroid on the Q -side, denoted with \mathbf{u}_Q , and dividing by the magnitude of the distance vector \mathbf{d}_j connecting the two cell centroids:

$$(\nabla \mathbf{u})_j \cdot \mathbf{A}_j = \frac{\mathbf{u}_Q - \mathbf{u}_P}{|\mathbf{d}_j|} |\mathbf{A}_j|.$$

For non-structured, non-orthogonal meshes (see Fig. 5), that are used in this work, an explicit non-orthogonal correction has to be added to the orthogonal component in order to preserve second order accuracy. See [29] for details.

A partitioned approach has been used to deal with the pressure-velocity coupling. In particular a Poisson equation for pressure has been used. This is obtained by taking the divergence of the momentum equation (5) and exploiting the divergence free constraint (2):

$$(22) \quad \Delta p = -\nabla \cdot (\mathbf{u} \otimes \mathbf{u}).$$

The segregated algorithms available in OpenFOAM[®] are SIMPLE [44] for steady-state problems, and PISO [28] and PIMPLE [41] for transient problems. For this work, we choose the PISO algorithm.

To discretize in time the equation (19), let $\Delta t \in \mathbb{R}$, $t^n = t_0 + n\Delta t$, with $n = 0, \dots, N_T$ and $t^* = t_0 + N_T\Delta t$. Moreover, we denote by \mathbf{u}^n the approximation of the flow velocity at the time t^n . We adopt Backward Differentiation Formula of order 1 (BDF1), see e.g. [47]. Given \mathbf{u}^n , for $n \geq 0$, we have, respectively,

$$(23) \quad \partial_t \mathbf{u} \approx \frac{\mathbf{u}^{n+1} - \mathbf{u}^n}{\Delta t},$$

Finally, a first-order scheme is also used for the discretization of the RCR Windkessel model (12):

$$(24) \quad \begin{cases} C_k \frac{p_{p,k}^{n+1} - p_{p,k}^n}{\Delta t} + \frac{p_{p,k}^{n+1}}{R_{d,k}} = Q_k^n, \\ p_k^{n+1} - p_{p,k}^{n+1} = R_{p,k} Q_k^n, \end{cases}$$

where we assumed $p_{d,k} = 0$.

2.3.4. Multi-scale coupling. The coupling process between the three-dimensional flow model and lumped Windkessel model can be summarized as follows:

- (1) At t^n , we know \mathbf{u}^n and thus Q_k^n . Then we calculate p_k^{n+1} by eq. (12);
- (2) We solve the problem (19)-(22) to obtain \mathbf{u}^{n+1} and Q_k^{n+1} .

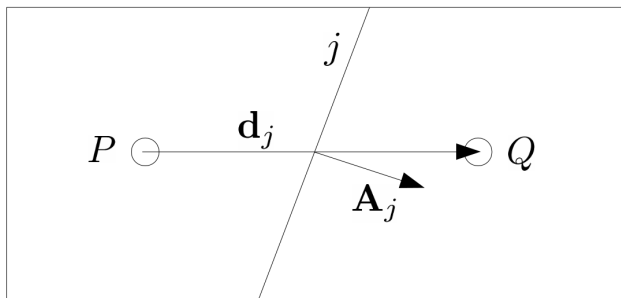


FIGURE 5. Close-up view of two non-orthogonal control volumes in a 2D configuration.

2.4. The reduced order model (ROM). The reduced order model we propose is the so-called *proper orthogonal decomposition with interpolation*. In Sec. 2.4.1 we provide a brief description of a such technique.

2.4.1. Proper orthogonal decomposition with interpolation. Proper orthogonal decomposition (POD) is a technique widely used within the reduced order modeling (ROM) framework for the study of parametric problems. POD allows to extract, from a set of high-dimensional snapshots, the basis minimizing the error between the original snapshots and their orthogonal projection. The data-driven approach here used is based only on data and does not require knowledge about the governing equations that describe the system. It is also non-intrusive, i.e. no modification of the simulation software is carried out. On the other hand, there are works that use non-intrusive methods that are not data-driven (see, e.g., [58]). The original snapshots are projected onto the POD space in order to reduce their dimensionality. Then the solution manifold is approximated using an interpolation technique. Several examples of applications based on this so-called POD with interpolation (PODI) [11] technique can be found in literature, in a wide range of contexts: naval engineering problems [16, 18, 17, 20], automotive [49, 22], aeronautics [48]. We also cite [24] where a coupling with isogeometric analysis is performed.

We are going to describe briefly the computation of the POD modes. We consider a problem with N degrees of freedom. Let φ_i , with $i = 1, \dots, N_s$, be the snapshots related to a generic variable of interest collected by solving the high-fidelity problem, with different values of the input parameters π_i , resulting in N_s input-output pairs (π_i, φ_i) . The snapshots matrix \mathbf{S} is built arranging the snapshots as columns, such that $\mathbf{S} = [\varphi_1, \varphi_2, \dots, \varphi_{N_s}]$. By applying the singular value decomposition to this matrix, we have:

$$(25) \quad \mathbf{S} = \mathbf{U}\mathbf{\Sigma}\mathbf{V}^* \approx \mathbf{U}_k\mathbf{\Sigma}_k\mathbf{V}_k^*,$$

where $\mathbf{U} \in \mathcal{A}^{N \times N_s}$ is the unitary matrix containing the left-singular vectors, $\mathbf{\Sigma} \in \mathcal{A}^{N_s \times N_s}$ is the diagonal matrix containing the singular values λ_i , and $\mathbf{V} \in \mathcal{A}^{N_s \times N_s}$, with the symbol $*$ denoting the conjugate transpose. The left-singular vectors, namely the columns of \mathbf{U} , are the so-called POD modes. We can keep the first k modes to span the optimal space with dimension k to represent the snapshots. The matrices $\mathbf{U}_k \in \mathcal{A}^{N \times k}$, $\mathbf{\Sigma}_k \in \mathcal{A}^{k \times k}$, $\mathbf{V}_k \in \mathcal{A}^{N_s \times k}$ in Eq. 25 are the truncated matrices with rank k .

After constructing the POD space, we can project the original snapshots onto this space. We compute $\mathbf{C} \in \mathcal{R}^{k \times N_s}$ as $\mathbf{C} = \mathbf{U}_k^T \mathbf{S}$, where the columns of \mathbf{C} are the so-called modal coefficients. We express the input snapshots as a linear combination of the modes using such coefficients. Then, we have:

$$(26) \quad \varphi_i = \sum_{j=1}^{N_s} \alpha_{ji} \phi_j \approx \sum_{j=1}^k \alpha_{ji} \phi_j, \quad \forall i \in [1, 2, \dots, N_s],$$

where α_{ji} are the elements of \mathbf{C} . Finally, we obtain the (π_i, α_i) pairs, for $i = 1, 2, \dots, N_s$, that sample the solution manifold in the parametric space. We are able to interpolate the modal coefficients α and for any new parameter approximate the new coefficients. At the end, we compute the high-dimensional solution by projecting back the (approximated) modal coefficients to the original space by using Equation 26. We remark that the procedure can be repeated for several variables of interests. Furthermore, it is not necessary for such a variable to be an unknown of the original system (such as velocity and pressure); indeed, we will use the PODI technique not only for primal quantities, but also for derived quantities such as WSS.

Regarding the technical implementation of the PODI method, we use the Python package called EZyRB [19].

3. NUMERICAL RESULTS AND DISCUSSION

We validate the FOM model both for pre-surgery and post-surgery configuration in Sec. 3.1. Then, we investigate the performance of the ROM model in Sec. 3.2.

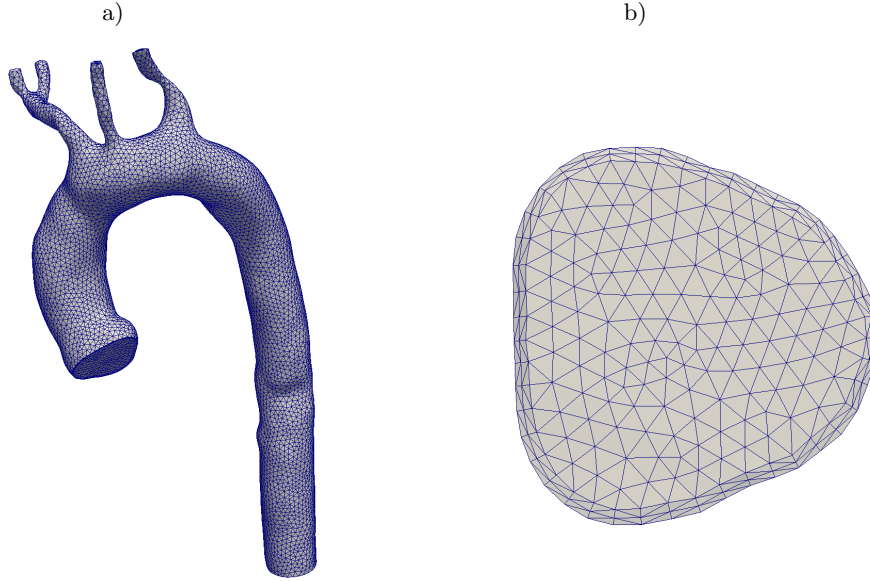


FIGURE 6. View of the mesh 230k: a) aortic wall, b) a section next to the aortic inlet.

mesh name	h_{min}	h_{max}	No. of cells
230k	5.8e-4	3e-3	228296
415k	5.6e-4	2.5e-3	414192
2000k	4.4e-4	1.5e-3	1993514

TABLE 10. Name, minimum diameter h_{min} , maximum diameter h_{max} , and number of cells for all the meshes used for the convergence study.

3.1. FOM validation. The number of PISO loops and non-orthogonal correctors has been fixed to 2 for all the simulations. The following solvers have provided a good compromise between stability, accuracy, and numerical cost. The linear algebraic system associated with eq. (19) is solved using an iterative solver with symmetric Gauss-Seidel smoother. Moreover, for Poisson problem (22), we use Geometric Agglomerated Algebraic Multigrid Solver GAMG with the Gauss-Seidel smoother. The required accuracy is 1e-6 at each time step.

3.1.1. Mesh convergence. In order to obtain grid independent solutions, we consider three meshes with tetrahedral elements. Table 10 reports name, minimum and maximum diameter, and number of cells for each mesh. Fig. 6 shows the mesh 230k. All the meshes under consideration have very low values of average non-orthogonality (around 30°) and skewness (around 1). The estimation of the Reynolds number is based on the diameter computed by considering the inlet areas, i.e. the ascending aorta (ao) section in the pre-surgery configuration and the outflow cannula section (oc) in the post-surgery configuration, as circular areas. We have

$$(27) \quad Re = \frac{Q}{A_{ao}} \sqrt{\frac{4A_{ao}}{\pi}} \frac{1}{\nu}$$

$$(28) \quad Re = \frac{PF}{A_{oc}} \sqrt{\frac{4A_{oc}}{\pi}} \frac{1}{\nu}$$

for the pre-surgery and post-surgery configuration, respectively. We carry out the mesh convergence study for the pre-surgery configuration because it is more critical with respect to the the post-surgery configuration being characterized by a greater Reynolds number Re as showed in Table 11. Moreover, note that in the pre-surgery configuration the Reynolds number is time dependent, with $0 \leq Re \leq 4200$.

	Re
Pre-surgery	[0, 4200]
Post-surgery: test 1	1818
Post-surgery: test 2	1862
Post-surgery: test 3	1995
Post-surgery: test 4	2217

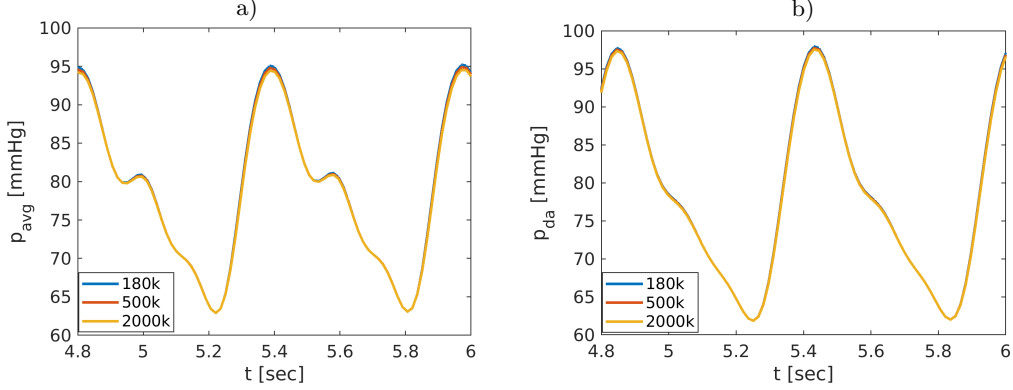
TABLE 11. Reynolds number Re for all the flow regimes under consideration.FIGURE 7. Pre-surgery configuration: time evolution on two cardiac cycles of the volume averaged arterial pressure p_{avg} as defined in (29) (a) and the pressure related to the descending aorta cross-section p_{da} (b) for the different meshes under consideration.

Fig. 7 compares the solution obtained with all the meshes reported in Table 10 both in terms of a global variable, the volume averaged arterial pressure, p_{avg} , defined as

$$(29) \quad p_{avg} = \frac{1}{\Omega} \int_{\Omega} p \, d\Omega,$$

and in terms of a local variable, the descending aorta cross-section pressure, p_{da} . We let the simulations run till transient effects are passed, $t^* \approx 8 \cdot T$. For a more quantitative comparison, we computed the Weighted Absolute Percentage Error (WAPE) ε [36] with respect to the solution obtained with the finer mesh 2000k:

$$(30) \quad \varepsilon = \frac{100}{n} \sum_{i=1}^n \left| \frac{X_i - X_i^{2000k}}{X^{2000k}} \right| \%,$$

where n is the number of sampling points, X_i is the solution related either meshes $230k$ and $415k$ at the i -th time step, X_i^{2000k} is the solution related to the mesh 2000k at the i -th time step and X^{2000k} is the time-averaged solution related to the mesh 2000k. For p_{avg} , we obtained $\varepsilon = 0.34\%$ for the mesh $230k$ and $\varepsilon = 0.16\%$ for the mesh $415k$. On the other hand, for p_{da} , we obtained $\varepsilon = 0.28\%$ for the mesh $230k$ and $\varepsilon = 0.13\%$ for the mesh $415k$. Thus, hereinafter, we will refer to the solutions computed by using the mesh $230k$. Regarding the post-surgery configuration, we choose a mesh with a similar refinement, having $200k$ cells, $h_{min} = 6.3e - 4$ and $h_{max} = 3.4e - 3$.

3.1.2. *Pre-surgery configuration.* The comparison between computational and experimental data is carried out in terms of systolic arterial pressure PAS , diastolic arterial pressure PAD and average arterial pressure PAM . Computational estimates of such quantities are evaluated by simulations in the following way:

$$(31) \quad PAS = \max_{t \in [0, T]} p_{avg},$$

$$(32) \quad PAD = \min_{t \in [0, T]} p_{avg},$$

$$(33) \quad PAM = \frac{1}{T} \int_0^T p_{avg} dt.$$

PAS (exp/num) [mmHg]	PAD (exp/num) [mmHg]	PAM (exp/num) [mmHg]
108/95.4	66/63.4	78/79.9

TABLE 12. Pre-surgery configuration: comparison between computational and experimental data.

Fig. 7 (a) shows the temporal evolution of p_{avg} (eq. (29)). Table 12 reports both numerical and experimental data marked by the abbreviations num and exp , respectively. We observe that the agreement is very good, within 11.7% for PAS , 4% for PAD and, 2.4% for PAM .

Fig. 8 displays the TAWSS magnitude distribution. Since in this case experimental data are not available, we just provide rough indications in order to justify the patterns obtained. Basically, we observe that peak values of TAWSS are localized in regions where narrowing of cross section happens or characterized by large curvature. On the other hand, regions characterized by lower TAWSS correspond to section enlargements. These results are expected by considering the classic findings for a straight cylindrical vessel with steady Poiseuille flow. In this simplified case, $WSS \propto 1/d^3$, where d is the pipe diameter. For biomedical experimental works that confirm such trend, the reader could see, e.g., [23, 42].

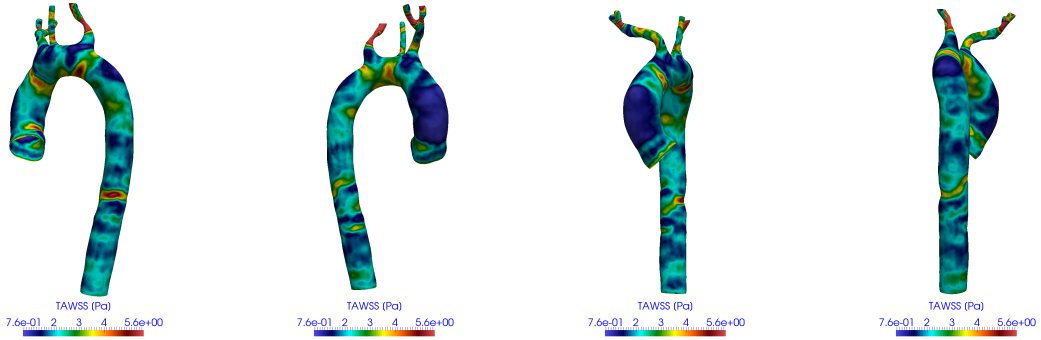


FIGURE 8. Pre-surgery configuration: TAWSS magnitude distribution on the entire wall of the model.

Fig. 9 a) depicts time averaged velocity streamlines. As expected, we note the generation of helical flow patterns in the aortic arch region (see, e.g. [35]).

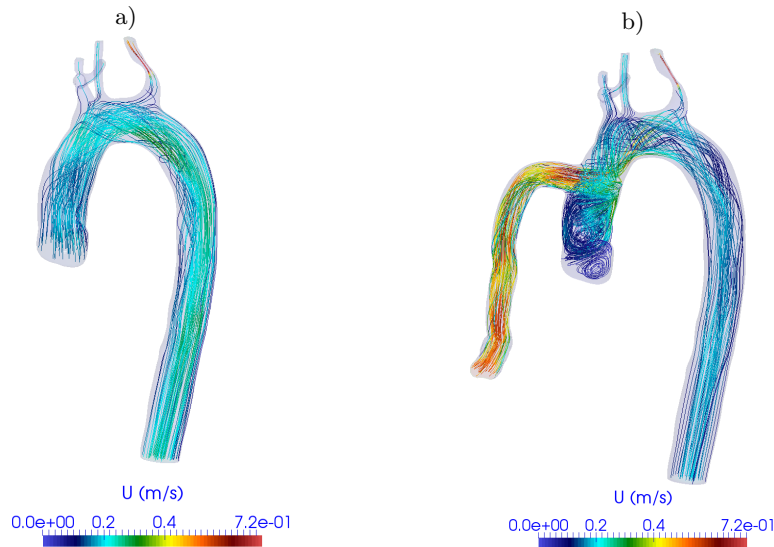


FIGURE 9. Velocity streamlines related to the pre-surgery configuration (a) and the post-surgery configuration for $PF = 4.1$ l/min and $\omega = 5400$ rpm (b).

PF [l/min]	PAM (exp/num) [mmHg]
4.1	78/78.6
4.2	90/90.6
4.5	100/100.7
5	83/82

TABLE 13. Post-surgery configuration: comparison between computational and experimental data.

3.1.3. *Post-surgery configuration.* Unlike the pre-surgery case, in the post-surgery configuration, since the LVAD flow rate is continuous and not pulsatile, and the aortic valve is closed, the solution is steady in time. Therefore, the comparison between computational and experimental data is based on a value only, $PAM = PAD = PAS$.

Table 13 reports both numerical (num) and experimental (exp) data for all the PF values considered. We observe that the agreement is excellent, within 1% in all the cases.

Figs. 10-13 show the WSS distribution for the three configurations investigated. As for the pre-surgery configuration, even in this case experimental data related to WSS are not available but it is possible to provide some interesting observations to be compared with previous works. In all the cases, we observe that there are high WSS, significantly greater than that obtained in the pre-surgery configuration, on the posterior region of the aortic arch, in front of the anastomosis. This high WSS zone is associated with the impingement of the jet from the cannula. This result is in agreement with those observed by [2, 13, 57]. Moreover we observe that elevated WSS also occur near the location of the outflow cannula, as found by [30, 31, 32, 38, 27, 10, 57]. On the contrary, on the most part of the aortic arch and descending aorta, very low WSS occurs. These patterns are critical from clinical viewpoints because highly heterogeneous WSS distribution coupled with the presence of a small region of the aortic arch exposed to high WSS could be associated to the development of atherosclerosis [21, 37]. Finally, we note that at increasing of PF from 4.1 to 5 l/min, the peak value of WSS moves from 12 to 15 Pa by following an almost linear trend.

Fig. 9 b) displays the velocity streamlines for the Test 1. With respect to the pre-surgery configuration, we observe that in the ascending aorta, below the anastomosis location, retrograde flow and recirculation zone are generated [13, 8, 30, 38, 2]. In addition, we observe that velocity values in the outflow cannula are higher than those in aorta because of its smaller diameter.

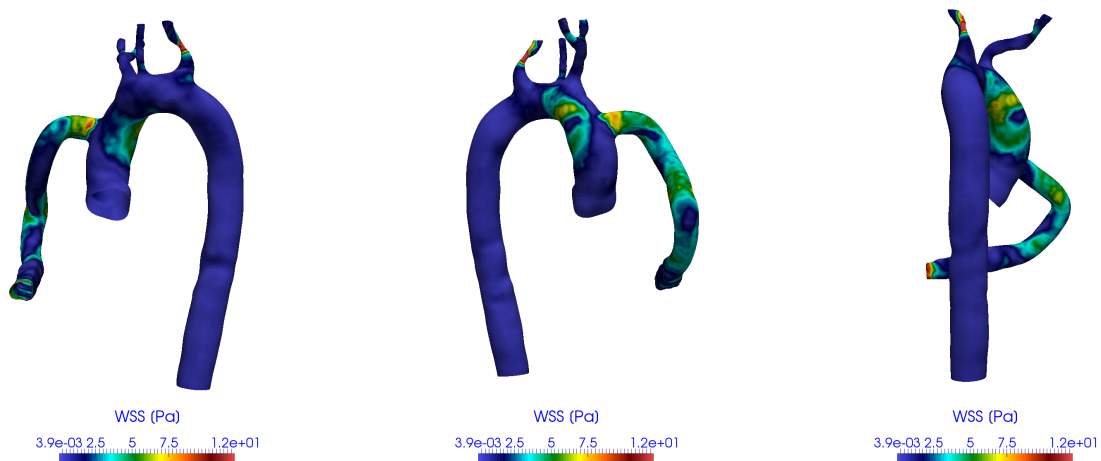


FIGURE 10. Post-surgery configuration: distribution of the WSS magnitude for $PF = 4.1$ l/min and $\omega = 5400$ rpm.

3.2. **ROM.** To train the ROM, the values of the LVAD flow rate, PF , are chosen using an equispaced distribution inside the range $PF \in [3, 5]$ that covers typical clinical values. Two sampling cases were considered. In the first case, we have 21 snapshots, and in the second one, 11 snapshots. Thus, the snapshots are collected every 0.1 in the first case and 0.2 in the latter one. For all the simulations, we use resistances and capacitances of Test 1 (see Tables 6, 7, 9). By assuming that we vary PF , and consequently ω , at a given $\Delta P = 75$ (see Table 5) and using the analytical fit 11, we obtain that the range $PF \in [3, 5]$ corresponds to $\omega \in [5076, 5720]$.

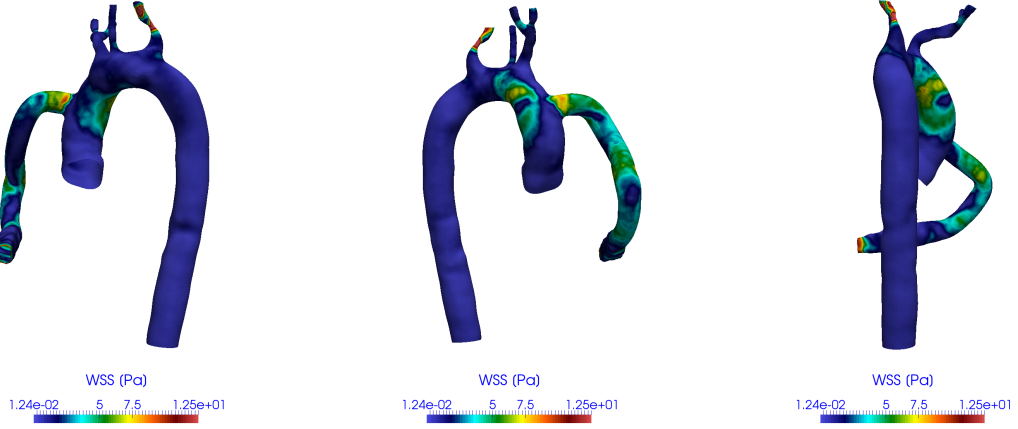


FIGURE 11. Post-surgery configuration: distribution of the WSS magnitude for $PF = 4.2$ l/min and $\omega = 5600$ rpm.

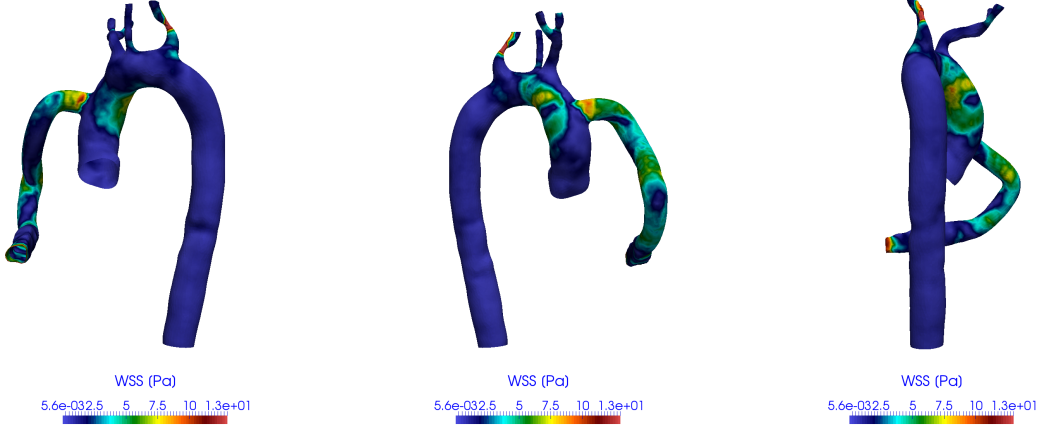


FIGURE 12. Post-surgery configuration: distribution of the WSS magnitude for $PF = 4.5$ l/min and $\omega = 6000$ rpm.

Two new values of the PF (ω) in which the ROM has not been trained but which belongs to the range of the training space, $PF = 3.45$ ($\omega = 5200$) and $PF = 4.35$ ($\omega = 5484$), are used to evaluate the performance of the parametrized ROM. POD modes and coefficients are computed as explained in Section 2.4.

Figure 14 shows the cumulative energy of the eigenvalues for pressure p , wall shear stress WSS, and velocity components, u_x , u_y and u_z . In order to retain the 99.9% of the system's energy, when we consider 21 snapshots, 1 mode for p , 14 for WSS, 16 for u_x , u_y and u_z are selected. On the other hand, when 11 snapshots are taken into account, 1 mode for p , 9 for WSS, 8 for u_x , u_y and u_z are selected. Moreover, to provide some quantitative results, the relative error in the L^2 -norm, calculated as

$$(34) \quad E_X = 100 \frac{\|X_{FOM} - X_{ROM}\|_{L^2(\Omega)}}{\|X_{FOM}\|_{L^2(\Omega)}} \%$$

where X_{FOM} is the value of a particular field in the FOM model, and X_{ROM} the one that is calculated using the ROM, is considered. In Tables 14 and 15, one could observe that the differences between the two spaces are minimal, for both the values of PF considered. Therefore, hereinafter results will be based on the database of 11 snapshots.

Figure 15 and 16 display a comparison between FOM and ROM for p and WSS fields, for both PF (ω) values under consideration. The comparison indicates that the ROM is able to provide a good reconstruction for both variables.

Figure 17 displays the velocity streamlines obtained both with FOM and ROM, and for both PF (ω) values under consideration. In order to further investigate the flow field, in Figure 18 a comparison between FOM

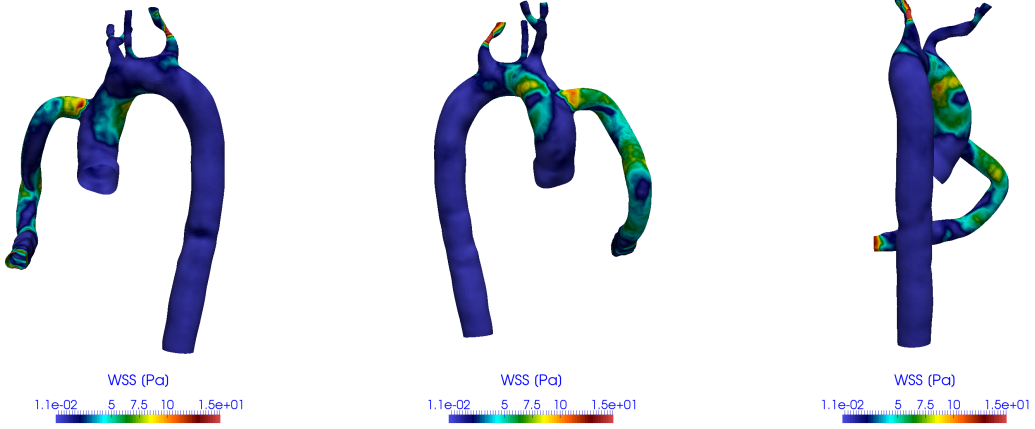


FIGURE 13. Post-surgery configuration: distribution of the WSS magnitude for $PF = 5$ l/min and $\omega = 5600$ rpm.

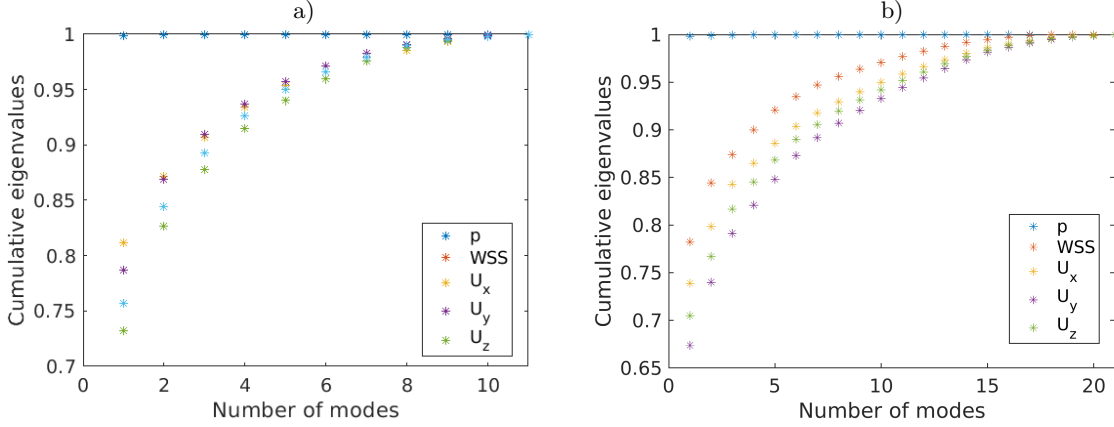


FIGURE 14. Cumulative energy of the eigenvalues for pressure p , wall shear stress WSS, and velocity components, u_x , u_y and u_z . The sampling frequency of the eigenvalues is 0.2 (a) and 0.1 (b).

	p	WSS	u_x	u_y	u_z
E_X (21 snapshots)	0.1%	4.1%	5.6%	7.9%	6.2%
E_X (11 snapshots)	0.2%	4.1%	5%	7.8%	5.8%

TABLE 14. L^2 norm relative errors for pressure p , wall shear stress WSS, and velocity components, u_x , u_y and u_z , to varying of the number of snapshots collected for $PF = 3.45$ l/min.

	p	WSS	u_x	u_y	u_z
E_X (21 snapshots)	0.2%	9.6%	10.7%	14.5%	10.5%
E_X (11 snapshots)	0.5%	7.2%	9.7%	13.5%	9.3%

TABLE 15. L^2 norm relative errors for pressure p , wall shear stress WSS, and velocity components, u_x , u_y and u_z , to varying of the number of snapshots collected for $PF = 4.35$ l/min.

and ROM for the velocity field related to a section of the ascending aorta next to the anastomosis location is shown. As observed for p and WSS fields, the ROM also performs well for the velocity.

The CPU time of the FOM model is 9600s and the one of the ROM is 40s. This corresponds to a speed-up of ≈ 240 , that demonstrates the fact that it is possible to use the ROM in the place of the FOM in order to obtain accurate simulations with a significant reduction of the computational cost.

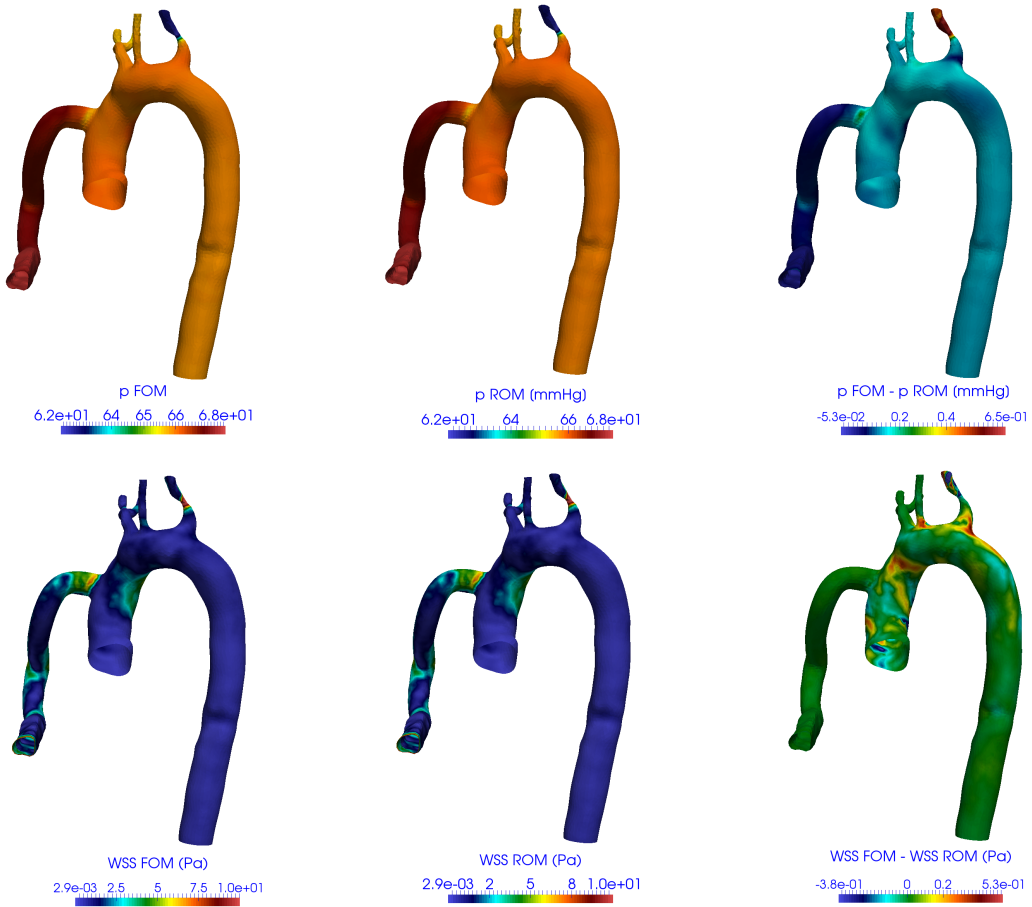


FIGURE 15. Comparison of the FOM/ROM pressure (1st row) and WSS (2nd row) at $PF = 3.45$ ($\omega = 5200$).

4. CONCLUSION AND PERSPECTIVES

In this work, a parametrized non-intrusive ROM using PODI method is used for the investigation of patient-specific aortic blood flow in presence of a LVAD device. The FOM is represented by the incompressible Navier-Stokes equations discretized by using a FV technique, coupled with three-element Windkessel models to enforce outlet boundary conditions. CT images of a patient are considered for the reconstruction of the geometry as well as RCH and ECHO data are exploited for the individualization of the three-element Windkessel models coefficients used to enforce boundary conditions. Therefore, a complete patient-specific framework is presented.

In order to showcase the features of our approach, we have successfully validated the FOM both for pre-surgery and post-surgery configuration by comparing numerical and experimental data. Then, the ROM developed is used to carry out a parametric study with respect to the LVAD flow rate. We show that the ROM provides accurate solutions with a significant reduction of the computational cost, up to at least two orders of magnitudes.

As a follow-up of the present work, we are going to investigate the influence of the LVAD device on the left and right ventricle flow patterns as well as their interaction. We are also interested in efficiently handling geometrical parametrization (e.g. in order to consider different anastomosis angles, or different designs of the outflow cannula) in the context of patient-specific geometries, extending e.g. the work carried out in [3] to different applications and different model reduction techniques.

Furthermore, we are designing an application that will be available online and allow computation to be run from standard web browsers.

5. ACKNOWLEDGEMENTS

We acknowledge the support provided by the European Research Council Executive Agency by the Consolidator Grant project AROMA-CFD "Advanced Reduced Order Methods with Applications in Computational

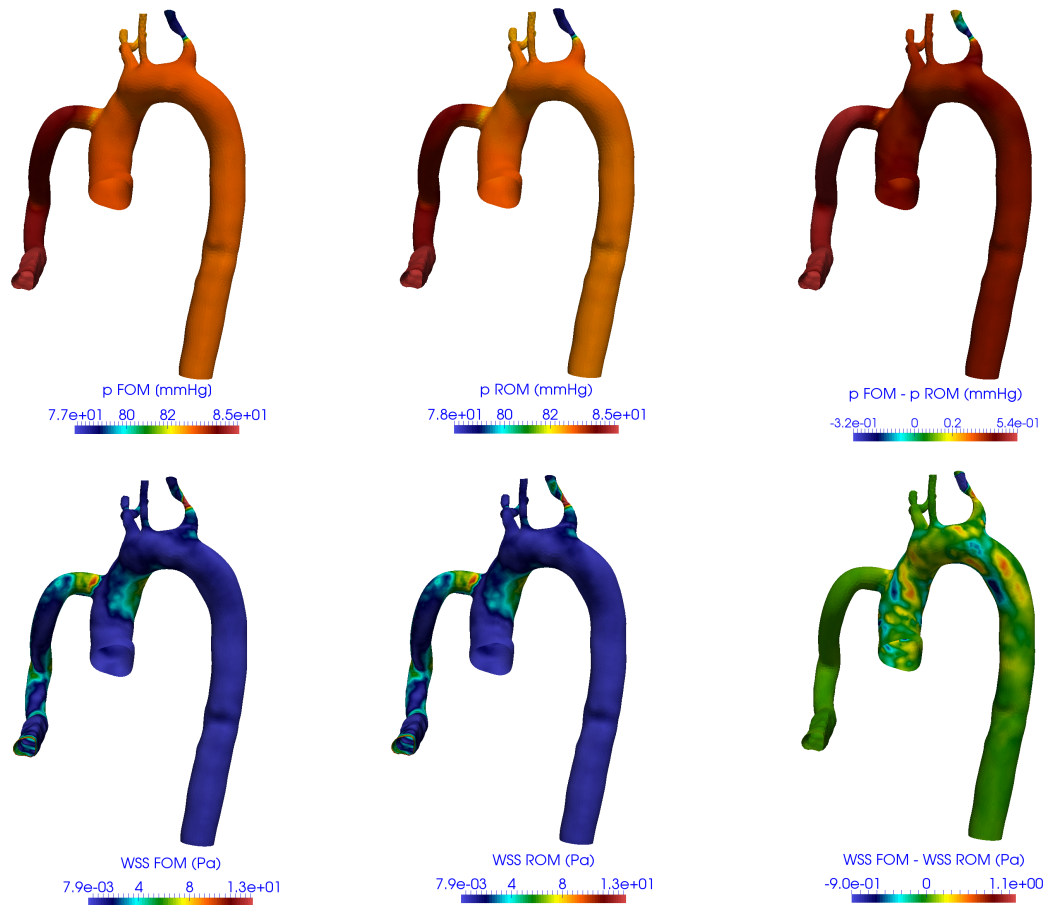


FIGURE 16. Comparison of the FOM/ROM pressure (1st row) and WSS (2nd row) at $PF = 4.35$ ($\omega = 5484$).

Fluid Dynamics” - GA 681447, H2020-ERC CoG 2015 AROMA-CFD and INdAM-GNCS 2020 project ”Tecniche Numeriche Avanzate per Applicazioni Industriali”.

REFERENCES

- [1] K. Aaronson, M. Slaughter, L. Miller, E. McGee, W. Cotts, M. Acker, M. Jessup, I. Gregoric, P. Loyalka, O. Frazier, V. Jeevanandam, A. Anderson, R. Kormos, J. Teuteberg, W. Levy, D. Naftel, R. Bittman, F. Pagani, D. Hathaway, and S. Boyce, *Heartware ventricular assist device (hvacd) bridge to transplant advance trial investigators. use of an intrapericardial, continuous-flow, centrifugal pump in patients awaiting heart transplantation*, *Circulation* **125** (2012), 3191–200.
- [2] A. Aliseda, V. K. Chivukula, P. McGah, A. R. Prisco, J. A. Beckman, G. J. M. Garcia, N. A. Mokadam, and C. Mahr, *LVAD outflow graft angle and thrombosis risk*, *ASAIO Journal* **63** (2017), no. 1, 14–23.
- [3] F. Ballarin, E. Faggiano, A. Manzoni, A. Quarteroni, G. Rozza, S. Ippolito, C. Antona, and R. Scrofani, *Numerical modeling of hemodynamics scenarios of patient-specific coronary artery bypass grafts*, *Biomechanics and Modeling in Mechanobiology* **16** (2017), no. 4, 1373–1399.
- [4] B. Barrick, A. Smeltz, A. Ganesh, H. Arora, and P. Kumar, *Aortic valve thrombus in a patient with an extracorporeal left ventricular assist device: The dilemma of management*, *Journal of Cardiothoracic and Vascular Anesthesia* **30** (2015).
- [5] Y. Bazilevs, J. Gohean, T. Hughes, R. Moser, and Y. Zhang, *Patient-specific isogeometric fluid–structure interaction analysis of thoracic aortic blood flow due to implantation of the jarvik 2000 left ventricular assist device*, *Computer Methods in Applied Mechanics and Engineering* **198** (2009), no. 45–46, 3534–3550.
- [6] P. Benner, M. Ohlberger, A. Pater, G. Rozza, and K. Urban, *Model Reduction of Parametrized Systems.*, vol. 1st ed. 2017, MS&A series, no. Vol. 17, Springer, 2017.
- [7] P. Benner, W. Schilders, S. Grivet-Talocia, A. Quarteroni, G. Rozza, and L. M. Silveira, *Model order reduction*, De Gruyter, Berlin, Boston, 2020.
- [8] J. Bonnemain, S. Deparis, and A. Quarteroni, *Connecting ventricular assist devices to the aorta: A numerical model*, pp. 211–224, Springer Milan, 2012.
- [9] J. Bonnemain, A. C. I. Malossi, M. Lesinigo, S. Deparis, A. Quarteroni, and L. Segesser, *Numerical simulation of left ventricular assist device implantations: Comparing the ascending and the descending aorta cannulations*, *Medical engineering & physics* **35** (2013), 1465–1475.

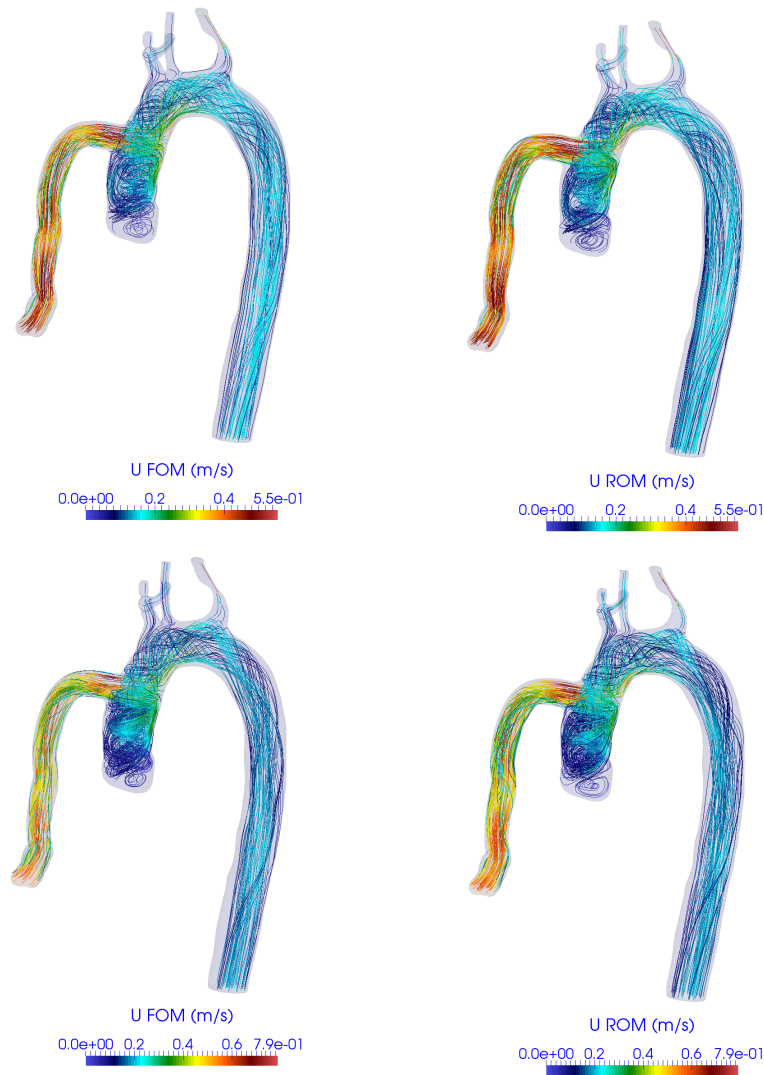


FIGURE 17. Comparison of the FOM/ROM velocity streamlines at $PF = 3.45$ ($\omega = 5200$) (1st row) and $PF = 4.35$ ($\omega = 5484$) (2nd row).

- [10] A. Brown, Y. Shi, A. Arndt, J. Miller, P. Lawford, and D. Hose, *Importance of realistic LVAD profiles for assisted aortic simulations: Evaluation of optimal outflow anastomosis locations*, Computer Methods in Biomechanics and Biomedical Engineering **15** (2011), 669–80.
- [11] T. Bui-Thanh, M. Damodaran, and K. Willcox, *Aerodynamic data reconstruction and inverse design using proper orthogonal decomposition*, AIAA Journal **42** (2004), 1505–1516.
- [12] C. Bulpitt, J. Cameron, C. Rajkumar, S. Armstrong, M. Connor, J. Joshi, D. Lyons, O. Moiola, and P. Nihoyannopoulos, *The effect of age on vascular compliance in man: Which are the appropriate measures?*, Journal of human hypertension **13** (1999), 753–8.
- [13] M. V. Caruso, V. Gramigna, M. Rossi, G. F. Serraino, A. Renzulli, and G. Fragomeni, *A computational fluid dynamics comparison between different outflow graft anastomosis locations of left ventricular assist device (LVAD) in a patient-specific aortic model*, International Journal for Numerical Methods in Biomedical Engineering **31** (2015), no. 2, e02700.
- [14] J. Crestanello, D. Orsinelli, M. Firstenberg, and C. Sai-Sudhakar, *Aortic valve thrombosis after implantation of temporary left ventricular assist device*, Interactive cardiovascular and thoracic surgery **8** (2009), 661–2.
- [15] Z. Demirozu and O. Frazier, *Aortic valve noncoronary cusp thrombosis after implantation of a nonpulsatile, continuous-flow pump*, Texas Heart Institute journal / from the Texas Heart Institute of St. Luke's Episcopal Hospital, Texas Children's Hospital **39** (2012), 618–20.
- [16] N. Demo, M. Tezzele, G. Gustin, G. Lavini, and G. Rozza, *Shape optimization by means of proper orthogonal decomposition and dynamic mode decomposition*, Technology and Science for the Ships of the Future: Proceedings of NAV 2018: 19th International Conference on Ship & Maritime Research, IOS Press, 2018, pp. 212–219.
- [17] N. Demo, M. Tezzele, A. Mola, and G. Rozza, *An efficient shape parametrisation by free-form deformation enhanced by active subspace for hull hydrodynamic ship design problems in open source environment*, The 28th International Ocean and Polar Engineering Conference, 2018.

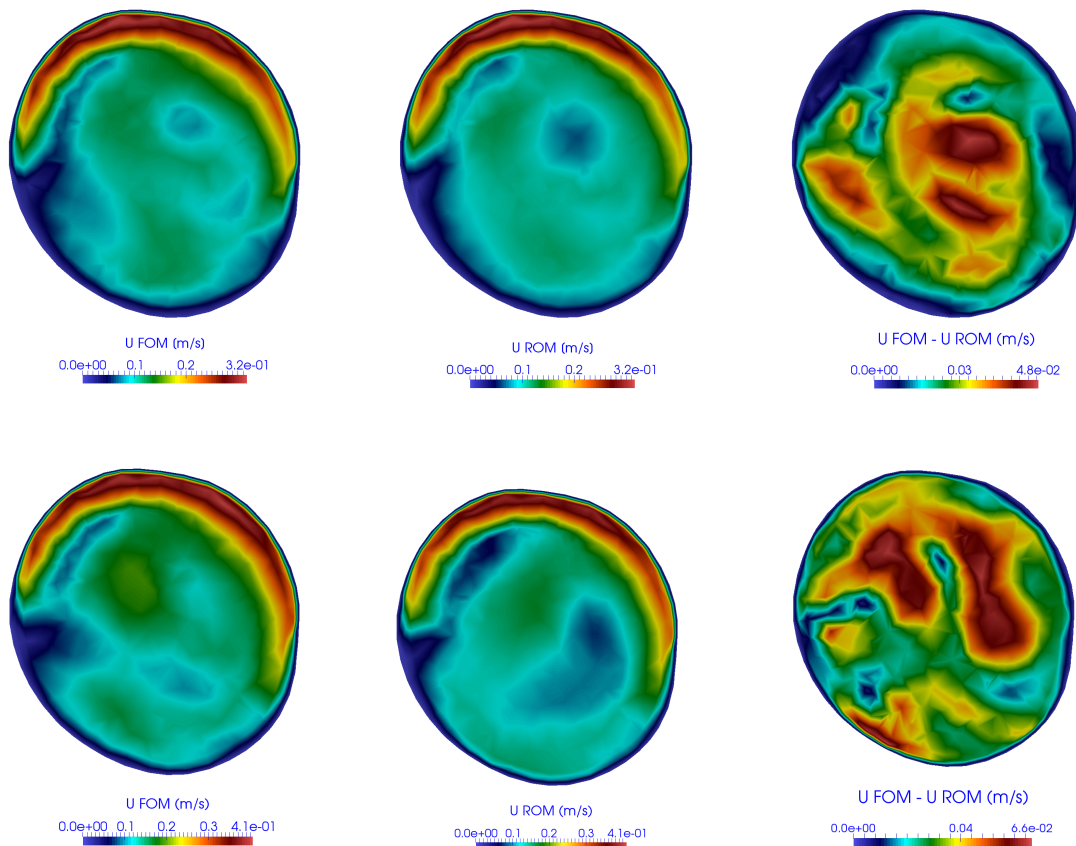


FIGURE 18. Comparison of the FOM/ROM velocity field related to a section of the ascending aorta next to the anastomosis location at $PF = 3.45$ ($\omega = 5200$) (1st row) and $PF = 4.35$ ($\omega = 5484$) (2nd row).

- [18] ———, *A complete data-driven framework for the efficient solution of parametric shape design and optimisation in naval engineering problems*, Proceedings of MARINE 2019: VIII International Conference on Computational Methods in Marine Engineering, 2019, pp. 111–121.
- [19] N. Demo, M. Tezzele, and G. Rozza, *EZyRB: Easy reduced basis method*, Journal of Open Source Software **3** (2018), 661.
- [20] N. Demo, M. Tezzele, and G. Rozza, *A non-intrusive approach for the reconstruction of POD modal coefficients through active subspaces*, Comptes Rendus Mecanique **347** (2019), no. 11, 873–881.
- [21] J. Dolan, H. Meng, S. Singh, R. Paluch, and J. Kolega, *High fluid shear stress and spatial shear stress gradients affect endothelial proliferation, survival, and alignment*, Annals of biomedical engineering **39** (2011), 1620–31.
- [22] V. Dolci and R. Arina, *Proper orthogonal decomposition as surrogate model for aerodynamic optimization*, International Journal of Aerospace Engineering **2016** (2016), 1–15.
- [23] E. Farag, P. Ooij, R. Plancken, K. Dukker, F. Heer, B. Bouma, D. Robbers-Visser, M. Groenink, A. Nederveen, B. Mol, J. Kluin, and S. Boekholdt, *Aortic valve stenosis and aortic diameters determine the extent of increased wall shear stress in bicuspid aortic valve disease: AS and aortic diameters determine WSS in BAV*, Journal of Magnetic Resonance Imaging **48** (2018).
- [24] D. Forti and G. Rozza, *Efficient geometrical parametrisation techniques of interfaces for reduced-order modelling: application to fluidstructure interaction coupling problems*, International Journal of Computational Fluid Dynamics **28** (2014).
- [25] J. Fried, J. Han, Y. Naka, U. Jorde, and N. Uriel, *Myocardial infarction after left ventricular assist device implantation: Clinical course, role of aortic root thrombus, and outcomes*, The Journal of heart and lung transplantation : the official publication of the International Society for Heart Transplantation **33** (2014), 112–5.
- [26] J. S. Hesthaven, G. Rozza, and B. Stamm, *Certified Reduced Basis Methods for Parametrized Partial Differential Equations*, Springer International Publishing, 2016.
- [27] G. Inci and E. Sorgüven, *Effect of LVAD outlet graft anastomosis angle on the aortic valve, wall, and flow*, ASAIO Journal **58** (2012), no. 4, 373–381.
- [28] R. I. Issa, *Solution of the implicitly discretised fluid flow equations by operator-splitting*, Journal of Computational Physics **62** (1986), no. 1, 40–65.
- [29] H. Jasak, *Error analysis and estimation for the finite volume method with applications to fluid flows*, Ph.D. thesis, Imperial College, University of London, 1996.

- [30] C. Karmonik, S. Partovi, M. Loebe, B. Schmack, A. Ghodsizad, M. R. Robbin, G. P. Noon, K. Kallenbach, M. Karck, M. G. Davies, A. B. Lumsden, and A. Ruhparwar, *Influence of LVAD cannula outflow tract location on hemodynamics in the ascending aorta: A patient-specific computational fluid dynamics approach*, *ASAIO Journal* **58** (2012), no. 6, 562–567.
- [31] C. Karmonik, S. Partovi, M. Loebe, B. Schmack, A. Weymann, A. B. Lumsden, M. Karck, and A. Ruhparwar, *Computational fluid dynamics in patients with continuous-flow left ventricular assist device support show hemodynamic alterations in the ascending aorta*, *The Journal of Thoracic and Cardiovascular Surgery* **147** (2014), no. 4, 1326–1333.
- [32] C. Karmonik, S. Partovi, B. Schmack, A. Weymann, M. Loebe, G. P. Noon, P. Piontek, M. Karck, A. B. Lumsden, and A. Ruhparwar, *Comparison of hemodynamics in the ascending aorta between pulsatile and continuous flow left ventricular assist devices using computational fluid dynamics based on computed tomography images*, *Artificial Organs* **38** (2014), no. 2, 142–148.
- [33] J. Kirklin, F. Pagani, R. Kormos, L. Stevenson, E. Blume, S. Myers, M. Miller, J. Baldwin, J. Young, and D. Naftel, *Eighth annual intermacs report: Special focus on framing the impact of adverse events*, *The Journal of Heart and Lung Transplantation* **36** (2017).
- [34] W. Laskey, H. Parker, V. Ferrari, W. Kussmaul, and A. Noordergraaf, *Estimation of total systemic arterial compliance in humans*, *Journal of Applied Physiology* (1985) **69** (1990), 112–9.
- [35] R. Lorenz, J. Bock, A. Barker, F. von Knobelsdorff, W. Wallis, J. Korvink, M. Bissell, J. Schulz-Menger, and M. Markl, *4D flow magnetic resonance imaging in bicuspid aortic valve disease demonstrates altered distribution of aortic blood flow helicity*, *Magnetic resonance in medicine* **71** (2014).
- [36] S. Makridakis, *Accuracy measures: theoretical and practical concerns*, *International Journal of Forecasting* **9** (1993), no. 4, 527 – 529.
- [37] A. Malek, *Hemodynamic shear stress and its role in atherosclerosis*, *JAMA* **282** (1999), 2035.
- [38] K. May-Newman, B. Hillen, and W. Dembitsky, *Effect of left ventricular assist device outflow conduit anastomosis location on flow patterns in the native aorta*, *ASAIO journal* **52** (2006), 132–9.
- [39] K. May-Newman, B. Hillen, C. Sirona, and W. Dembitsky, *Effect of LVAD outflow conduit insertion angle on flow through the native aorta*, *Journal of medical engineering & technology* **28** (2004), 105–9.
- [40] R. Mazzitelli, F. Boyle, E. Murphy, A. Renzulli, and G. Fragomeni, *Numerical prediction of the effect of aortic left ventricular assist device outflow-graft anastomosis location*, *Biocybernetics and Biomedical Engineering* **36** (2016), no. 2, 327–343.
- [41] F. Moukalled, L. Mangani, and M. Darwish, *The finite volume method in computational fluid dynamics: An advanced introduction with OpenFOAM and Matlab*, 1st ed., Springer Publishing Company, Incorporated, 2015.
- [42] P. Ooij, M. Markl, J. Collins, J. Carr, C. Rigsby, R. Bonow, S. Malaisrie, P. McCarthy, P. Fedak, and A. Barker, *Aortic valve stenosis alters expression of regional aortic wall shear stress: New insights from a 4dimensional flow magnetic resonance imaging study of 571 subjects*, *Journal of the American Heart Association* **6** (2017), e005959.
- [43] A. F. Osorio, R. Osorio, A. Ceballos, R. Tran, W. Clark, E. A. Divo, I. R. Argueta-Morales, A. J. Kassab, and W. M. DeCampi, *Computational fluid dynamics analysis of surgical adjustment of left ventricular assist device implantation to minimise stroke risk*, *Computer Methods in Biomechanics and Biomedical Engineering* **16** (2013), no. 6, 622–638.
- [44] G. V. Patankar and D. B. Spalding, *A calculation procedure for heat, mass and momentum transfer in three-dimensional parabolic flows*, *International Journal of Heat and Mass Transfer* **15** (1972), no. 10, 1787–1803.
- [45] A. Quaini, S. Canic, and D. Paniagua, *Numerical characterization of hemodynamics conditions near aortic valve after implantation of left ventricular assist device*, *Mathematical biosciences and engineering* **8** (2011), 785–806.
- [46] A. Quarteroni, A. Manzoni, and F. Negri, *Reduced Basis Methods for Partial Differential Equations*, Springer International Publishing, 2016.
- [47] A. Quarteroni and G. Rozza, *Numerical solution of parametrized Navier–Stokes equations by reduced basis methods*, *Numerical Methods for Partial Differential Equations* **23** (2007), no. 4, 923–948.
- [48] M. Ripepi, M. Verveld, N. Karcher, T. Franz, M. Abu-Zurayk, S. Grtz, and T. Kier, *Reduced-order models for aerodynamic applications, loads and mdo*, *CEAS Aeronautical Journal* **9** (2018).
- [49] F. Salmoiraghi, A. Scardigli, H. Telib, and G. Rozza, *Free-form deformation, mesh morphing and reduced-order methods: enablers for efficient aerodynamic shape optimisation*, *International Journal of Computational Fluid Dynamics* **32** (2018), no. 4-5, 233–247.
- [50] Y. Shi, P. Lawford, and D. Hose, *Numerical modeling of hemodynamics with pulsatile impeller pump support*, *Annals of biomedical engineering* **38** (2010), 2621–34.
- [51] M. Slaughter, J. Rogers, C. Milano, S. Russell, J. Conte, D. Feldman, B. Sun, A. Tatoes, R. Delgado, J. Long, T. Wozniak, W. Ghumman, D. Farrar, O. Frazier, and A. Ehsan, *Advanced heart failure treated with continuous-flow left ventricular assist device*, *The New England journal of medicine* **361** (2009), 2241–51.
- [52] M. Tezzele, N. Demo, A. Mola, and G. Rozza, *An integrated data-driven computational pipeline with model order reduction for industrial and applied mathematics*, In press, Special Volume ECMI (W. Schilders ed.) (2020).
- [53] Thoratec Corporation, *HeartMate 3 left ventricular assist system: Instructions for use*, 2017.
- [54] H. G. Weller, G. Tabor, H. Jasak, and C. Fureby, *A tensorial approach to computational continuum mechanics using object-oriented techniques*, *Computers in physics* **12** (1998), no. 6, 620–631.
- [55] N. Westerhof, J.-W. Lankhaar, and B. Westerhof, *The arterial Windkessel*, *Medical & biological engineering & computing* **47** (2008), 131–41.
- [56] T. Zbigniew, D. Obidowski, and K. Jozwik, *Numerical analysis of the VAD outflow cannula positioning on the blood flow in the patientspecific brain supplying arteries*, *Mechanics and Mechanical Engineering* **22** (2018), 619–635.
- [57] Q. Zhang, B. Gao, and Y. Chang, *Helical flow component of left ventricular assist devices (LVADs) outflow improves aortic hemodynamic states*, *Medical Science Monitor* **24** (2018), 869–879.
- [58] X. Zou, M. Conti, P. Dez, and F. Auricchio, *A non-intrusive proper generalized decomposition scheme with application in biomechanics*, *International Journal for Numerical Methods in Engineering* **113** (2017).